Solar Wind Electron Parameters Determination on Wind Spacecraft Using Quasi-Thermal Noise Spectroscopy

Mihailo Martinović, Kristopher Klein, Savannah Gramze, Himanshu Jain, Milan Maksimović, Arnaud Zaslavsky, Chadi Salem, Ioannis Zouganelis, Zoran Simić

▶ **To cite this version:**

Mihailo Martinović, Kristopher Klein, Savannah Gramze, Himanshu Jain, Milan Maksimović, et al.. Solar Wind Electron Parameters Determination on Wind Spacecraft Using Quasi-Thermal Noise Spectroscopy. Journal of Geophysical Research Space Physics, 2020, 125 (8), 10.1029/2020JA028113 . hal-03251916

HAL Id: hal-03251916
https://hal.science/hal-03251916

Submitted on 25 Jun 2022

HAL is a multi-disciplinary open access archive for the deposit and dissemination of scientific research documents, whether they are published or not. The documents may come from teaching and research institutions in France or abroad, or from public or private research centers.

L'archive ouverte pluridisciplinaire **HAL**, est destinée au dépôt et à la diffusion de documents scientifiques de niveau recherche, publiés ou non, émanant des établissements d'enseignement et de recherche français ou étrangers, des laboratoires publics ou privés.

Copyright

Check for updates

JGR Space Physics

TECHNICAL REPORTS: METHODS
10.1029/2020JA028113

Solar Wind Electron Parameters Determination on Wind Spacecraft Using Quasi-Thermal Noise Spectroscopy

Mihailo M. Martinović[1,2], Kristopher G. Klein[1], Savannah R. Gramze[1], Himanshu Jain[1], Milan Maksimović[2], Arnaud Zaslavsky[2], Chadi Salem[3], Ioannis Zouganelis[4], and Zoran Simić[5]

[1]Lunar and Planetary Laboratory, University of Arizona, Tucson, AZ, USA, [2]LESIA, Observatoire de Paris, Meudon, France, [3]Space Sciences Laboratory, University of California, Berkeley, CA, USA, [4]European Space Agency, ESAC, Madrid, Spain, [5]Astronomical Observatory of Belgrade, Belgrade, Serbia

Abstract Quasi-thermal noise (QTN) spectroscopy has been extensively used as an accurate tool to measure electron density and temperature in space plasmas. If the antenna length to radius ratio is sufficiently large, a typical measured spectrum clearly shows a resonance at the electron plasma frequency and a lower frequency plateau that quantify the electron distributions. The Wind spacecraft, with its long, thin antennas, is considered the mission par excellence for the implementation of the QTN method. However, a major issue in applying QTN spectroscopy is contamination from signals other than the ubiquitous plasma noise in the vicinity of plasma frequency, affecting the measured spectra and confusing their physical interpretation. In this work, we present a new method for selecting the observations of uncontaminated QTN, distinguishing it from other plasma and spacecraft effects. The selected measurements are used to obtain accurate values for both thermal and suprathermal electron parameters. Testing of the method on 1.5M observations under various conditions in the solar wind, including slow and fast wind and solar transients, confirms the reliability and accuracy of the method with no systematic flaws.

Key Points:
- Wind spacecraft quasi-thermal noise (QTN) spectra is filtered to independently measure electron core and halo parameters
- An automated algorithm accounts for a variety of sources of signal contamination, allowing the processing of large numbers of QTN spectra
- Electron density and core temperature are determined with an accuracy of the order of 5% for over 75 days of solar wind observations

Correspondence to:
M. M. Martinović,
mmartinovic@email.arizona.edu

Citation:
Martinović, M. M., Klein, K. G., Gramze, S. R., Jain, H., Maksimović, M., Zaslavsky, A., et al. (2020). Solar wind electron parameters determination on Wind spacecraft using quasi-thermal noise spectroscopy. *Journal of Geophysical Research: Space Physics*, *125*., e2020JA028113. https://doi.org/10.1029/2020JA028113

Received 18 APR 2020
Accepted 24 JUN 2020
Accepted article online 17 JUL 2020

©2020. American Geophysical Union. All Rights Reserved.

1. Introduction

Understanding the physics of the solar wind and other weakly collisional plasma environments depends on high-quality in situ measurements of electron and ion distributions. Comprehensive data sets of such measurements are provided by several kinds of electrostatic analyzers flown on various missions (Bame et al., 1978; Lin et al., 1995; Sauvaud et al., 2008; Schwenn et al., 1975; Whittlesey et al., 2020; Young et al., 2004), but these measurements suffer from multiple limiting factors, such as varying spacecraft electrostatic potential (Henri et al., 2011; Pulupa et al., 2014), secondary electron emission (Kellogg, 1981; Whipple et al., 1969), and temporal variations of the instrument internal calibrations (Laframboise & Parker, 1973). Quasi-thermal noise (.) spectroscopy depends on the level of electrostatic plasma fluctuations around the plasma frequency (Andronov, 1966; Fejer & Kan, 1969) and is therefore not influenced by the systematic issues affecting electrostatic analyzers. A standard QTN spectra, for a dipole antenna arm length L_{ant} longer than the local Debye length L_D, consists of three spectral regions (Meyer-Vernet & Perche, 1989): (1) a thermal plateau at $f < f_p$, where signal scales with $\sqrt{T_c}$, (2) a plasma resonance peak just above f_p, and (3) a signal scaling with total plasma pressure and logarithmically decreasing with frequency above f_p. Here, $\omega_p = 2\pi f_p = \sqrt{n_e e_c^2/\epsilon_0 m_e}$ is the electron plasma frequency, ϵ_0 is the dielectric permeability of vacuum, and n_e, e_c, and m_e are the total electron density,and its charge and mass, respectively, while T_c is the temperature of the thermal part of the electron velocity distribution function (VDF).

QTN spectroscopy was first applied to high frequency spectrum measured by ISEE-3 four decades ago (Meyer-Vernet, 1979). Since then, the method has been improved to include the effects of suprathermal electrons (Couturier et al., 1981; Meyer-Vernet & Perche, 1989), specific electron VDFs (Chateau & Meyer-Vernet, 1989; 1991; Le Chat et al., 2009; Zouganelis, 2008), ions (Issautier et al., 1996, 1999; Meyer-Vernet et al., 1986), strong magnetic field (Sentman, 1982; Meyer-Vernet et al., 1993; Moncuquet et al., 1997), or electron-neutral collisions (Balmain, 1969; Martinović et al., 2017). It was recognized that measurement quality can be affected due to instrumental limitations, such as dipole antenna arms separation (Meyer-Vernet & Perche, 1989; Meyer-Vernet et al., 2017) or geometry (Martinović et al., 2015) and the usage of

short and/or thick antennas, which significantly enhance electron impact noise (Maksimović et al., 2005; Martinović et al., 2016; Le Chat et al., 2013).

These limitations are minimized on the Wind Thermal Noise Receiver (TNR), which consistently measures a clearly visible plasma peak. This is because its dipole antenna arms satisfy $L_{\mathrm{ant}}/L_D \sim 5$ and have a very small antenna radius $L_{\mathrm{ant}}/a_{\mathrm{ant}} \sim 10^5$, making the shot noise negligible (Martinović, 2016) and the thermal plateau clearly distinguishable in the vast majority of observations. These characteristics enable the straightforward identification of resonant peaks in typical TNR QTN spectra, enabling the use of peak tracking methods for the estimation of n_e and T_c (Issautier et al., 2005; Salem et al., 2003) and cross-calibration with particle detectors (Maksimovic et al., 1998; Salem et al., 2003). Independent fits of both thermal and suprathermal electron parameters that use all three QTN spectral regions have also been performed on individual spectra from both Wind and Ulysses (Issautier et al., 1999; Maksimovic et al., 1995).

The next step in analyzing TNR measurements was processing the entire data set in a similar fashion. However, this task proved to be complicated, for several reasons. First, the spacecraft spin can affect the proton contribution to the spectrum at low frequencies, and modeling this effect is theoretically challenging and numerically time consuming (Tong et al., 2015). Second, there are multiple signals that contaminate QTN spectra in different spectral regions that vary with plasma conditions, including ion acoustic-like waves at $f \ll f_p$ (Salem et al., 2003), Langmuir waves at f_p (Vidojević et al., 2011), second harmonic emission at $2f_p$ (Cairns, 1986), or galactic center emission at $f \gg f_p$ (Hillan et al., 2010). If any of the measured TNR frequency channels is affected by these phenomena, using that particular channel will lead to an overestimation of plasma temperature. The same processes can give rise to additional peaks in the spectrum, with similar shape and amplitude to the genuine plasma peak, possibly causing a peak tracking algorithm to fail and produce catastrophic errors in estimating n_e. Due to these technical difficulties, an automated algorithm that could be reliably used throughout the mission has not yet been developed.

The development of such an algorithm that will allow for the processing of the entire Wind data set is the focus of this work. We introduce a novel method that filters a TNR spectrum, using only the frequency channels where an uncontaminated QTN signal is measured, without any interference from other plasma processes, celestial bodies, or the spacecraft. In order to make the method independent of other electron measurements on Wind, we designed the peak tracking procedure that finds multiple peaks within the spectrum and selects the correct plasma peak through the system of quality flags (QFs) or grades. These QFs inform us of the "goodness" of a particular spectrum for a given set of plasma parameters, providing input for of fitting the filtered observations according to QTN theory. The details of the method are provided in Section 2 and Appendix A1. We then proceed to verify method under various conditions in the solar wind, demonstrating its accuracy in slow and fast wind streams, compression regions, and Interplanetary Coronal Mass Ejections (ICMEs, Section 3), finding n_e and T_c with an uncertainty of 3–5% and suprathermal parameters with an accuracy of ∼10% for halo temperature and ∼30% for halo density. When compared with electron VDF moments provided by the two Wind particle analyzers, the Solar Wind Experiment Vector Electron and Ion Spectrometer (SWE VEIS) (Ogilvie et al., 1995) and 3-Dimensional Plasma Electron Electrostatic Analyzer (3DP EESA) (Lin et al., 1995), these results showed a very good agreement for values of n_e and satisfying agreement for total electron temperature T_e. In Section 4, we examine the statistical properties of a 75-day data set, comparing it to previous analysis and finding good agreement. In the future, we will process the entire TNR data set in this fashion, measuring the properties of electron VDFs over two solar cycles. We will also use these measurements to examine the properties of electron VDFs around interplanetary shocks at high cadence and complement other comprehensive studies in this field (Wilson et al., 2019).

2. Method

The TNR is a part of Wind/Waves radio receiver, which is equipped with a wire dipole antenna, each arm $L_{\mathrm{ant}} = 50$ m long and $a_{\mathrm{ant}} = 0.19$ mm in diameter (Bougeret et al., 1995). The receiver is sampling at 96 logarithmically spaced frequency channels between 4 and 256 kHz in 4.4% resolution, using five 32-channel bands (A–E). Channels A, C ,and E fully cover the entire frequency range and the instrument most frequently operates using these channels in the so-called ACE regime. Channels B and D overlap with the other three and are used occasionally for plasma peak determination by an on board neural network. Even though the neural network has the primary purpose of locating the plasma peak, it can be unreliable in the fast solar

wind spectra and is not used in our analysis. Within a 4.4-s measurement cadence in the ACE regime, the sampling time for each channel is determined by the time needed to produce statistical variations of less than 0.3 dB (~7.2%). Considering typical plasma VDF fluctuations during the acquisition time interval at 1 au are reaching up to few percent (Chen et al., 2014; Bowen et al., 2018; Kellogg et al., 2009), we further on assume that the measurement uncertainties are ~10%. The time reserved for each band is 1.472 s, while the actual acquisition time within this interval varies for each band (Bougeret et al., 1995), and the time left after the acquisition is used for performing on board fast Fourier transforms and data storage. Approximately 19,600 spectra are produced each day, for a total of about 180 million observations over Wind's 25-year duration.

The synthetic QTN spectrum V^2 is calculated using contributions from electrons V^2_{qtn}, protons V^2_{pn} and antenna gain Γ as

$$V^2 = \Gamma^2\left(V^2_{\mathrm{qtn}} + V^2_{\mathrm{pn}}\right). \tag{1}$$

Due to the antenna being very long and thin, with $L_{\mathrm{ant}}/a_{\mathrm{ant}} > 10^5$, the effects of impact noise can be completely neglected (Martinović, 2016). The electron QTN is estimated using the model of double Maxwellian electron VDF, composed of an isotropic core of density n_c and temperature T_c, and an isotropic halo of density n_h and temperature T_h. Details of the procedure are given by Couturier et al. (1981), with expressions for the antenna capacitance, electron noise, and antenna gain in Eq. B16, B19 and 14, respectively. Here, we briefly review the general spectrum properties important for our analysis method:

1. The synthetic electron spectrum is effectively flat at $f < f_p$, with $V^2_{\mathrm{qtn}} \sim \sqrt{T_c}$.
2. The plasma peak appears at frequencies a few percent above f_p, with the peak height linearly increasing with $\tau_h = T_h/T_c$ and width increasing with $a_h = n_h/n_c$.
3. The synthetic electron spectrum drops with frequency as $V^2_{\mathrm{qtn}} \sim f^{-3}$ for $f \gg f_p$ and scales with the total plasma pressure $V^2_{\mathrm{qtn}} \sim n_e\sqrt{T_e}$.

Proton parameters are taken from Wind/SWE Faraday cup measurements (Ogilvie et al., 1995). Proton noise V^2_{pn}, important below f_p, is calculated using the expression for the solar wind velocity $\mathbf{v_{sw}}$ being perpendicular to the Waves antenna, given by Eq. 22 of Issautier et al. (1999). This approach is, of course, approximate, as the spacecraft is spinning with period 3 s, and the acquisition time is shorter than the half of spin period, so the angle between antenna and $\mathbf{v_{sw}}$ can affect the measured spectrum. We neglect this effect for three reasons. First, Tong et al. (2015) showed that the proton contribution is significant only at very low frequencies and when the antenna to v_{sw} angle is smaller than 15°. Second, the model of the proton noise for an arbitrary angle is very computationally demanding and would be impractical for a tool designed to process a large set of data. Third, the accuracy of the minimum identification used in the analysis is unaffected by this approximation; only the number of selected filtered channels below f_p is affected.

The initial step in our method is the determination of possible plasma peaks. For each measured QTN spectrum, we apply a simple peak tracking algorithm; for a given spectrum, we find up to five local maxima $V^2_{\mathrm{TNR}}(p)$, where $p \in [0,95]$ is an integer that locates the maximum data point. To be considered a maxima, the point must satisfy the following conditions:

$$V^2_{\mathrm{TNR}}[p] > V^2_{\mathrm{TNR}}[p+1] > V^2_{\mathrm{TNR}}[p+2] > V^2_{\mathrm{TNR}}[p+3] > V^2_{\mathrm{TNR}}[p+4], \tag{2}$$

$$V^2_{\mathrm{TNR}}[p] > V^2_{\mathrm{TNR}}[p-1], \tag{3}$$

$$V^2_{\mathrm{TNR}}[p] > V^2_{\mathrm{TNR}}[p-2] + 0.2\ \mathrm{dB}. \tag{4}$$

The condition in Equation 4 prevents occasionally measured wave-like signals at low frequencies from appearing as false peaks. In our analysis of 1.5M observations, described in Section 4, no spectra with more than four maxima that satisfy Equations 2–4 were found, so we conclude that finding up to five local maxima with our algorithm is sufficient to locating the plasma peak in any realistic TNR spectrum. We sweep the spectrum over the range $f \in$ 4.9–158.1 kHz, equivalent to electron densities $n_e \in$ 0.3–308 cm^{-3}. For each peak $V^2_{\mathrm{TNR}}[p]$, we determine the corresponding value of $n_{e(\mathrm{init})}$, computed not from the frequency related to $V^2_{\mathrm{TNR}}[p]$, but $V^2_{\mathrm{TNR}}[p-1]$, due to property (2). Five linearly spaced values of n_e between $n_{e(\mathrm{init})}$ and $1.04n_{e(\mathrm{init})}$ are considered, taking into account the TNR's finite resolution.

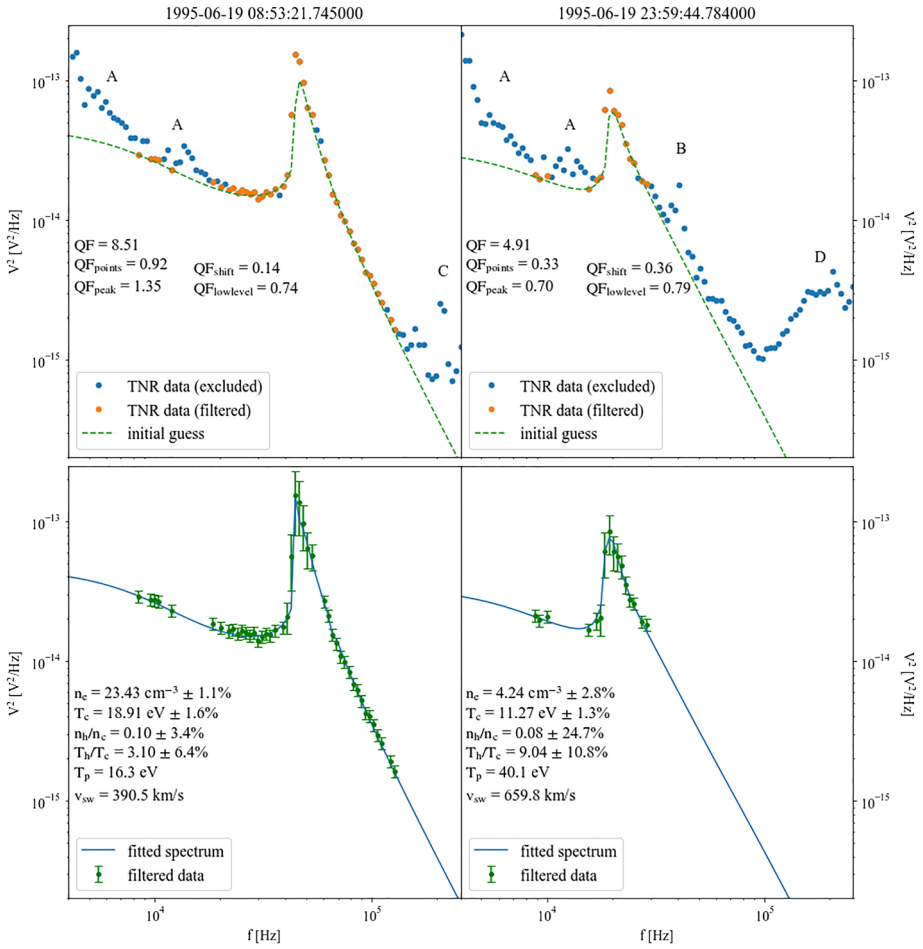

Figure 1. Example of the TNR spectra from slow (left) and fast (right) solar wind. The data filtering method is illustrated in the top panels, with selected frequency channels given in orange. The initial guess used for fitting (dashed lines) is the synthetic spectrum with the highest evaluated total QF. For determination of the fitted parameters and their respective uncertainties (bottom panels), the estimated errors of both theory and observation are taken into account. The major characteristic of the fitting method is that number and confidence of measurements around the plasma peak strongly affect the measurement uncertainties of the suprathermal parameters. Signals not originating from QTN are labeled by capital letters as follows: (A) proton noise modulation due to spacecraft spinning, (B) $2f_p$ resonance, (C) galactic radiation, and (D) AKR.

We next calculate synthetic QTN spectra V^2, assuming a single electron Maxwellian VDF ($a_h = 0$), for each of the five n_e values for each of the five peaks. Starting from $T_c = 2$ eV and increasing it by 1 eV for each synthetic spectrum, we determine the highest core temperature such that $V^2 < V^2_{\mathrm{TNR}}$. Therefore, the initial temperature, $T_{c(\mathrm{init})}$, is found with a numerical accuracy of 1 eV. The same procedure is repeated for temperatures between $T_{c(\mathrm{init})}$ and $T_{c(\mathrm{init})} + 1$ eV in increments of 0.1 eV. It is important to emphasize that, due to properties (1) and (3), the frequency at which the synthetic spectrum exceeds the measured one can appear either below or above f_p. In this step, we neglect an excess of the theoretical spectrum above the observed spectrum for frequency values in the interval $[0.97,1.1]f_p$ the due to possible numerical inaccuracies in the gain calculation close to the peak. If a theoretical excess appears in this region, we do not take it into account and continue until it is encountered somewhere else in the spectrum. This approach turns out to be very important in the fast solar wind, where densities tend to be low and considerable wave activity is frequently observed (Salem et al., 2003), leaving few or no data points that measure only the QTN thermal plateau. This approach is essential to resolving errors in of peak tracking and temperature determination that affected both the Wind/Waves neural network and previous analysis methods, as observing only the plateau below f_p and the peak properties is not enough to confidently resolve n_e and T_c in about 10% of the fast solar wind spectra.

Finally, we use property (2) to estimate the halo electron parameters. The plasma peak can only increase, at least for realistic solar wind plasma parameters, with increasing a_h and τ_h (Couturier et al., 1981). We start with $a_h = 0$, and increase this ratio by 0.01 per iteration. For each iteration, we set $\tau_h = 0$, and increase τ_h by 1, calculating QFs for each set of n_e, T_c, a_h, and τ_h parameters, until the synthetic spectrum exceeds the measured one, as described in Appendix A1, when the iteration ends and the next value of a_h is used. When the measured spectra is exceeded even for $\tau_h = 0$, the value of n_e is processed and the algorithm moves to the next one.

At the end of this process, we obtain up to 25 sets of QFs, each containing up to several hundred values, for different a_h and τ_h. The parameter combination (n_e, T_c, a_h, τ_h) that corresponds to the highest QF, along with the filtered frequency channels (see Appendix A1 and Figure 1 for a description of the method for determining which frequency channels are excluded from the fit), is used as an input to a standard Levenberg-Marquardt fitting method, providing final values of these VDF moments and their uncertainties. When estimating measurement errors, we take into account the inaccuracy of both model and observation very close to f_p by increasing the uncertainties of the data points as given by Equation A1.

3. Results

The left panels in Figure 1 show a TNR spectrum measured from the slow solar wind, with a slightly increased density compared to standard conditions at 1 au (Issautier et al., 2005; Wilson et al., 2019). Aside from galactic radiation above 100 kHz (C) and increased signal at low frequencies, likely originating from spacecraft spinning effects (A), the QTN signal is clearly visible in a wide region around f_p. Increased density implies $L_{\text{ant}}/L_D \approx 8$, producing a very intensive plasma peak, which in turn provides tight constraints for suprathermal parameters a_h and τ_h. We note this spectrum is from the edge of a compression region (Figure 2), where measurements from particle detectors could possibly exhibit a decreased level of confidence; indeed the Faraday cup measurement shows $n_p + 2n_\alpha \approx 17.84\ \text{cm}^{-3}$, significantly different from the $23.34\ \text{cm}^{-3}$ extracted from our method. As the most confident peak obtained in our algorithm provides approximate $n_{e(\text{init})}$ that is more than 25% different than this value, it is flagged as suspicious, and the total QF, calculated using Equation A3, is decreased by 1. Regardless of this penalty on the QF, the spectrum is still evaluated as highly reliable, and we show it as an example of QTN spectroscopy providing an improvement to particle measurements in a solar transient event.

The right panels of Figure 1 illustrate a typical TNR spectrum observed in a fast solar wind stream close to the L1 point (the spacecraft was definitively stationed at the L1 point in 2004, while in this example, it was just temporarily passing through this region). Here, we encounter the same difficulties as in the previous example, as well as additional contamination from the $2f_p$ emission (B) and auroral kilometric radiation (AKR) (D). The secondary peak is eliminated by the algorithm as a possible primary plasma resonance, but its contribution to the measured power spectral density significantly decreases the number of available data points to fit. The plasma peak is still resolvable but is smaller than in the previous case as $L_{\text{ant}}/L_D \approx 4.3$. Here, we note that, although the peak visibility is fairly approximated using L_{ant}/L_D value, it is also determined by a_h and τ_h (Couturier et al., 1981). Lower electron density also yields fewer frequency channels available below f_p, most of which are for this spectrum almost completely unusable. However, the algorithm still detects few conveniently grouped points in the thermal plateau, which are sufficient to obtain reliable values of T_c. A major difference compared to the slow wind example is the uncertainties in the suprathermal parameters a_h and τ_h. As the relative density a_h is mostly determined from the peak width with respect to its center, the confidence level is strongly affected both by a lack of data points from the cutoff on the left side of the peak and its low overall height. This issue was also encountered in previous studies (Issautier et al., 1999; Maksimovic et al., 1995) on Ulysses Unified Radio and Plasma Wave (URAP) data at larger radial distances. URAP was equipped with long and thin antennas and measured QTN spectra shapes very similar to the ones shown in Figure 1 but without the secondary peak at $2f_p$, and the uncertainty on a_h was of the same order of magnitude as in this study. The temperature ratio τ_h is dominantly determined by the peak intensity compared to the signal at the thermal plateau, keeping the relative error at the order of 10% for vast majority of the results (Figure 5).

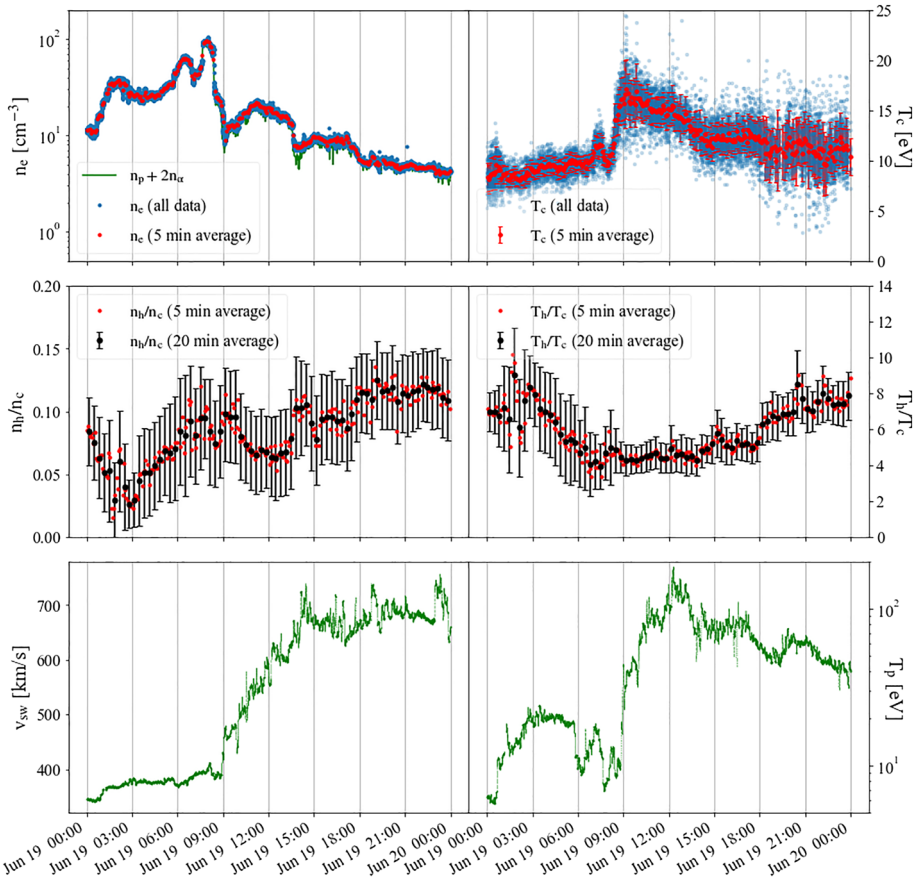

Figure 2. Best fit parameters from 19 June 1995. Top panels illustrate densities and temperatures, with the full time cadence measurements of n_e and T_c given by blue dots. For both thermal and suprathermal parameters in top and middle panels, 5- and 20-minute averages with standard deviations, as a proxy for uncertainties, are given by red and black dots, respectively. For n_e averages, uncertainties are of the order of a dot size, and results are in very good with agreement with values of $n_p + 2n_\alpha$, except at the edges of the ICME just before 09:00 (Figure 1, left) and just before 14:00, where discrepancy of up to 30% can appear. Standard deviations of a_h and τ_h (middle panels) are fairly constant throughout the day, being of the order of 25% and 10%, respectively, for stable conditions over the averaging interval. These deviations are decreased only in the solar transient, due to very intensive plasma peak. Faraday cup ion density, bulk velocity, and temperature are given by green solid lines in the top left and bottom panels.

Figure 2 shows results for an example day that has a several illustrative periods: a steady slow wind stream that until 09:00, a compression region around 11:00, followed by a solar transient lasting until approximately 14:30, and a steady fast wind stream for the rest of the day. The total density estimation (top left panel), based on peak tracking, shows confident results throughout the day with measurement uncertainty of the order of the instrument resolution (~4.4%), while the 5-min averages are of the order of 1% for a steady stream during the interval (Figure 5). Measurements of T_c, plotted on the top right panel, also show very low average values of fitted parameters uncertainties, being ~4% in the slow and ~6% in the fast wind (the error bars shown are larger than these values, as they do not represent the fit uncertainties, but standard deviations during 5-min periods). These highly accurate results are possible only when the thermal plateau is recognized correctly and consistently, removing contamination of the QTN spectra from other sources and leaving the instrument precision as the only limiting factor. Uncertainties of suprathermal parameters, determined from the peak shape, are considerably larger, with average values of ~25% for Δa_h and ~10% for $\Delta\tau_h$ (middle panels). As the peak quality is primarily determined by the L_{ant}/L_D ratio, a_h and τ_h values are more confined for the measurements where the density is high and the plasma conditions are not changing rapidly. The time periods 03:00–05:00 and 10:00–13:00 are examples of such steady behavior, showing that the spread of 5-min averages is very similar to the spread of 20-min averages of same quantities, as we reach the

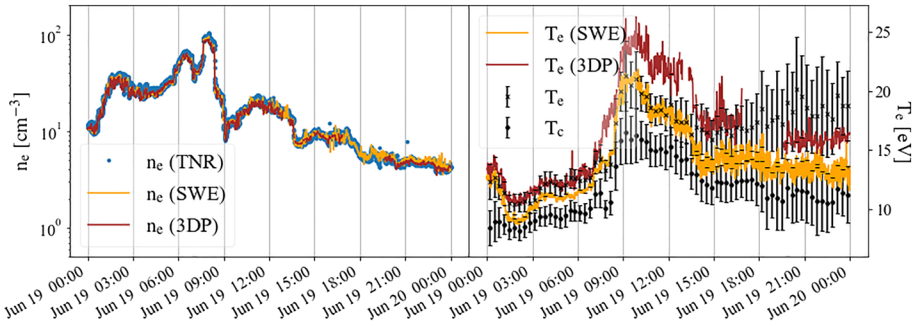

Figure 3. Comparison of total electron density (left) and total electron temperature (right) between TNR (blue for the entire data set and black for 20-min averages), SWE (orange), and 3DP (brown). The values of n_e match within a few percent, while for T_e, the level of agreement between the data sets varies with solar wind conditions. The T_c results from Figure 2 (top right) are replotted for comparison and are systematically lower than the values from all three data sets.

instrument accuracy threshold. However, it must be emphasized that unique measurements of a_h or t_c are, generally, not sufficiently accurate without taking into account the surrounding values.

Figure 3 shows a comparison of n_e and T_e obtained using our method with the results provided by the SWE and 3DP instrument teams. Here, the total electron temperature is calculated in a standard manner for a VDF consisted of two Maxwellians

$$T_e = T_c \frac{1 + a_h \tau_h}{1 + a_h}. \tag{5}$$

We obtain a very strong agreement between the the total density values, which is not surprising considering that the electron analyzer data is calibrated with the plasma peak measured by TNR. However, values of T_e show considerable discrepancy with each other, while having satisfying agreement with our results in certain plasma streams. In the slow wind, TNR values have very low uncertainties and are very close to the ones given by 3DP. This agreement continues in the fast wind, but not in the compression region and the ICME, where TNR and SWE values are very close to each other. It is worth emphasizing that the uncertainties ΔT_e are dominantly determined by Δa_h, as this parameter has the least confident one in our data set. Therefore, measurements in the fast solar wind, and in a low density plasma in general, are limited by the lower amplitude of the plasma peak. Under these conditions, the information that we can obtain about the peak shape is limited, leading to larger measurement errors.

4. Application to a Larger Data Set

The method described in Section 2 is designed to be applicable to the entire TNR data set, containing approximately 180 million measurements collected during Wind's quarter of a century mission lifetime. An analysis of this entire data set is left for future work; here, we process 75 days of solar wind measurements, from 13 April to 26 June 1995. In this period, TNR made 1,526,734 measurements, 1,350,515 (88.4%) of which were successfully processed by our algorithm, producing initial guesses for fit parameters. Levenberg-Marquardt fitting converged in 1,229,643 (91%) cases, providing usable values of plasma parameters, while the rest of the measurements did not satisfy the conditions related to QF_{peak}, defined in Appendix A1.

In Figure 4, we show the derived electron characteristics. It is important to note that, for a majority (64%) of measurements, less then 32 out of 96 data points are classified as measured "pure" QTN signal. This result is not surprising, as significant regions of the TNR frequency range, both above and below f_p, are persistently covered by contamination from other signals, as described above. Results in the top right panel illustrate the statement made in Section 2 that the initial value of T_c needs to be estimated using the entire TNR spectrum instead of only the part below f_p. If it was not the case, all the cases where the synthetic spectrum exceeds the measured one at $f > f_p$ would be rejected by our algorithm to avoid overestimation of initial T_c.

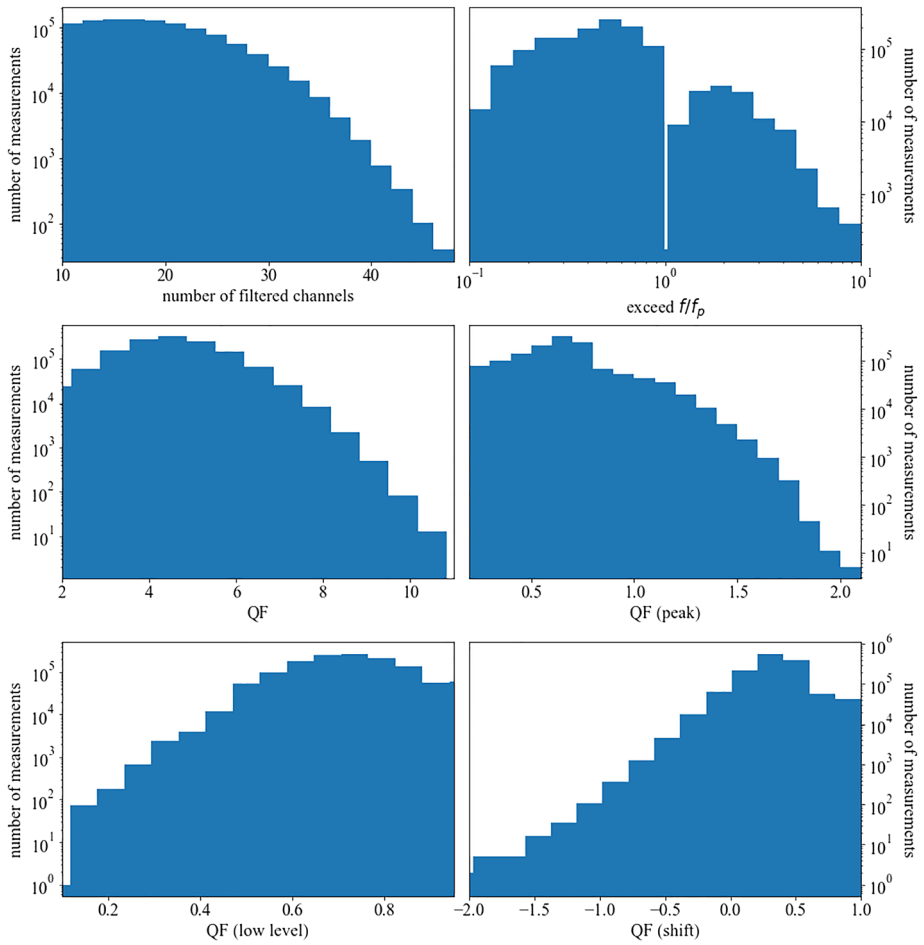

Figure 4. Overview of the quality flags statistics. Occurrence distributions of QF_{points} (shown as number of filtered TNR channels), QF and $QF_{lowlevel}$, shown in panels on the left, are exponentially decreasing from their most probable values, as it is expected for random processes. On the other hand, appearance of exceed frequencies above f_p, QF_{peak} and QF_{shift} are related to traces of different physical processes detected by the receiver, and as such, to a good approximation, exhibit a power law shape.

The distribution of peak QF testifies to the very good overall measurement quality, with constant decrease of the signal, starting from the plasma peak, extending to approximately $1.5f_p$ for the largest fraction of measurements, while it can reach up to $5f_p$ in rare occasions. This property serves as an additional verification of the successful peak tracking, as possible false peaks are cut off by the conditions defined in Appendix A1. Another sanity check is provided by the $QF_{lowlevel}$ distribution (bottom left). We examine our initial T_c with 0.1eV linear accuracy. On the other hand, there is a square root dependency $V^2 \sim \sqrt{T_c}$ below f_p, causing our normal distribution to peak at $\sqrt{2}/2$ instead of 0.5. This randomly distribution impacts the global QF results, with the addition of a tale at QF > 9.5, which originates from very high values of QF_{peak}. The same parameter causes the "practical maximum" QF = 10, defined in Appendix A1, to be exceeded in a handful of cases. This feature is not corrected as only 22 (0.0016%) of the calculated QFs are larger than 10. Finally, QF_{shift} provides a valuable information on the limitations of the method. The negative values seen on bottom right panel appear when artificially added peak frequency channels (Appendix A1) have intensities significantly above the synthetic spectrum. The cause of this discrepancy can be a population of very fast electrons, which cannot be modeled by a Maxwellian halo and highly enhances the plasma peak (Chateau & Meyer-Vernet, 1989, 1991; Le Chat et al., 2009). Since the power-law-shaped VDFs are common in the solar wind at 1 au, the correction is forced in 72.4% of all measurements.

Analysis of both core and halo density uncertainties shown in Figure 5 is in agreement with the results shown in the left panels of Figure 1. While the bulk of T_c and τ_h uncertainties are centered around ~10%,

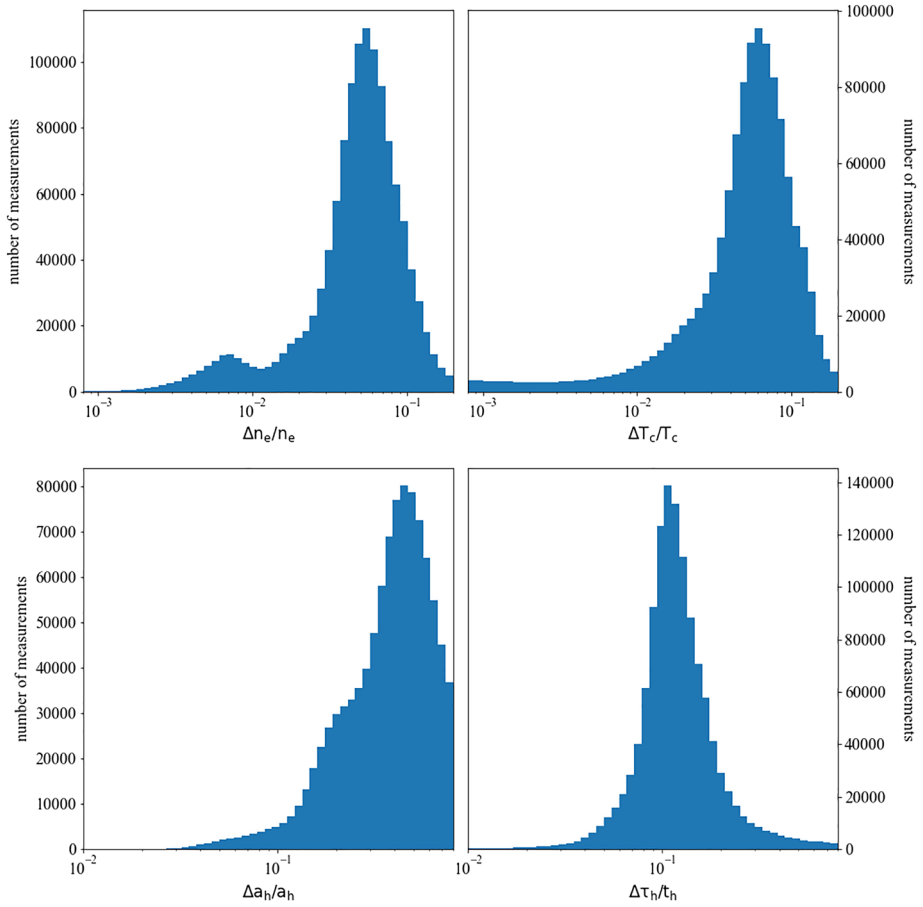

Figure 5. Histograms of relative errors of measured plasma VDF moments. Relative uncertainties of n_e are not physical, but asymmetric distribution of uncertainty in a_h originates from reduced measurement errors in periods when plasma peak is very intense (L_{ant}/L_D ratio is increased).

the value determined by the instrument characteristics, both n_e and a_h distributions show tails significantly below the most probable values. These measurements originate from periods when n_e is higher and/or T_c is lower than usually measured in the solar wind, and the L_{ant}/L_D ratio induces a very intense plasma peak with a large number of data points available. On the other hand, cases when $\Delta n_e < 1\%$ are caused by the fitting method finding a very sharp local minimums due to specific shape of some of the filtered spectra. These error estimates are unrealistic as they are below the instrument thresholds and should not be considered reliable.

In Figure 6, we compare two-dimensional histograms from SWE and 3DP with our results. All three instruments agree with a well-known lack of correlation between n_e and T_e at 1 au. Any significant correlation between these quantities would be an indication of potential flaws in our method. Pearson product-moment correlation coefficients between n_e and T_e are −0.16 for 3DP data and −0.06 for SWE data. The same coefficient for TNR data is −0.21 but drops down to −0.06 for $n_e - T_c$ correlation (results in the bottom panel). This discrepancy appears because a_h values obtained by our method have larger spread for lower densities then the ones obtained by particle analyzers. This is an expected result, due to both less intense plasma peaks measured for this region of the parameter space and limitations of the double Maxwellian VDF used in our model. The QTN spectrum close to f_p is very sensitive to small fractions of very fast electrons, which are better described by power-law-like distributions (Maksimović et al., 1997; Wilson et al., 2019). The fitting process therefore detects these high intensities and evaluates increased values of the suprathermal parameters to get the best possible fit. A natural way of removing this difficulty is usage of κ distributions for halo component, which was the initial approach in our method, using results from

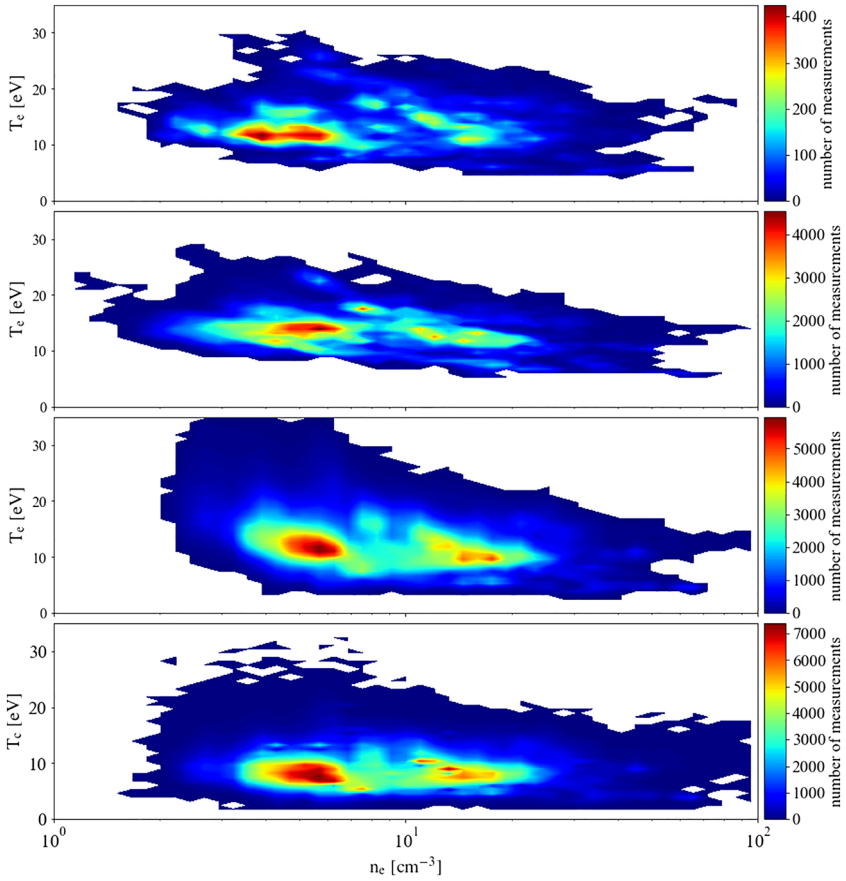

Figure 6. Histograms (from top to bottom) of 3DP, SWE and TNR T_e and T_c, for 75 days from 13 April to 26 June 1995. None of the data sets show any notable correlation between n_e and T_e, while our method could be slightly overestimating electron total temperature when density is very low.

Le Chat et al. (2009). However, TNR signal saturates so quickly with the number of fast electrons that the κ exponent as a new parameter has uncertainties so large that the results were not confident and are highly biased by the initial guess. In more than 90% of cases examined, the fitted value of κ remained within 5% of the arbitrarily chosen initial guess. This problem appeared previously in Ulysses data processing (Le Chat et al., 2011). The same low-density periods are related to the largest uncertainties of τ_h, which additionally contributes to the spread of the results. The method of constraining τ_h using signal ratio between the plasma peak and the low-frequency plateau was applied successfully by Moncuquet et al. (2020) to Parker Solar Probe (PSP) Fields measurements where electron halo was very low, but for the case of Wind TNR, data do not bring an improvement to our method due to non-negligible values of a_h at 1 au.

5. Summary and Conclusions

The Wind TNR instrument has accumulated an extensive data set of ~180 million QTN spectra during the last two and a half decades. This number is expected to increase to over half a billion until the end of the mission (Spann et al., 2017). In order maximally utilize this large archive of observations, it is necessary to develop an automated algorithm that provides electron VDF moments from electric field fluctuations power spectra using QTN spectroscopy.

The technical details of the algorithm are presented in Section 2 and Appendix A1. In Section 3, we have tested it on one specific day, 19 June 1995, during which Wind was sampling several different solar wind regimes. The major features of the method, including the estimation of n_e and T_c from plasma peak tracking

and minimum of the measured signal, remain confident and highly accurate throughout various plasma conditions. We note that the confidence of the results for suprathermal components is dependent on the strength of the plasma peak. Uncertainty in these parameters does remain below or on the order of 25% throughout the surveyed data set. Results of Section 4 confirm that our method provides sensible results when applied to a 75-day long time span of observations. We apply additional statistical tests, to check for possible hidden artificial effects on our results, and show that there is no unphysical correlation between independent parameters n_e and T_c, Figure 6, and the uncertainties and QFs have the expected statistical distributions for Gaussian and power-law shapes for random errors, Figure 5, and appearances of physical phenomena, Figure 4, bottom panels, respectively.

Finally, it is worth discussing several possible contributions to the measured spectra that are not addressed by our model. First, when the electron VDF differs significantly from the sum of two Maxwellians, the theoretical spectrum might not adequately correspond to observations in certain frequency domains. The presence of electron beam or "strahl," expected to be directed outward in the quiescent solar wind (Štverak et al., 2009; Berčič et al., 2019) and bidirectional in large-scale flux-rope strictures (Gosling et al., 1987), is expected to, according to preliminary calculations, be important just below the plasma peak. The possible effect on our results is a slight overestimation of a_h parameter in streams with strong strahl, usually observed in the fast solar wind. The same study suggests that the affection of halo anisotropy is minimal for ratio between parallel and perpendicular components of T_h is smaller then 7, which is almost always the case at 1 au, and should be below the instrument sensitivity for a spinning spacecraft. Second, characteristic flat-top VDFs have been observed in the magnetosheath of Earth (Chateau & Meyer-Vernet, 1989) and around quasi-perpendicular shocks (Wilson et al., 2019). Generation these structures is not fully understood, with electric field fluctuations due to cross-shock electrostatic potential being a candidate process (Feldman et al., 1983; Hull et al., 1998; Morse, 1965). This type of distribution is also characterized by increased number of very fast electrons and produces similar effects as κ distributions—an enhanced plasma peak (Martinović et al., 2017) that can cause potential overestimation of t_h. Third, in the magnetosphere and geomagnetic tail of Earth, where Wind spends nonnegligible amount of time prior to 2004, the magnetic field is increased compared to the solar wind, and electron cyclotron frequency becomes comparable to plasma frequency. In this scenario, the signal shape at the thermal plateau below f_p changes to a wave-like signal with minimums at positive integer multipliers of the electron cyclotron frequency (Meyer-Vernet, 1982; Sentman, 1982). Extracting of T_c from the signal minimums is still possible using our method (Moncuquet et al., 1995), but the resonant frequency needs to be adjusted to upper hybrid instead of plasma frequency (Balmain, 1969). The QTN features inside the bowshock are not relevant for the results presented here but will need to be addressed in processing of the entire mission data set. Finally, as noted in Section 2, Wind/Waves long and thin antennas make the contribution of the impact noise, which is not fully understood and the least accurately measured factor in QTN spectroscopy, completely negligible. Usage of the method presented here on instruments equipped with short and thick antennas, such as PSP Fields (Bale et al., 2016) and Solar Orbiter Radio and Plasma Waves (Maksimović et al., 2020), is possible but requires implementation of the impact noise effects at lower frequencies. This task was previously successfully done for STEREO measurements (Martinović et al., 2016; Zouganelis et al., 2010), but a confident numerical model of impact noise at $f \approx f_p$ (Meyer-Vernet, 1983) is not developed and is a topic for future work.

In summary, the method presented in this work provides accurate values of total electron density and core temperature in any plasma conditions, along with providing confident results for the suprathermal components. Due to providing results at a substantially higher cadence than Wind particle analyzers, we will use it as a tool to examine electron VDFs around structures, such as interplanetary shocks. Modifications of the algorithm presented here are required for adequate processing of the specific environments, such as Earth magnetosphere, magnetosheath, or magnetic clouds. These adjustments are left for future projects, where we will process the entire database of TNR measurements and make it available to the community.

Appendix A: Calculating a QTN Spectrum QFs

We define a QF as a measure of the reliability of a measured spectrum V^2_{TNR} with respect to a given QTN synthetic spectrum V^2. It depends on a set of input plasma parameters n_e, T_c, a_h, τ_h, T_p, and v_{sw} that uniquely define V^2.

Prior to rating any TNR spectrum with any QTN synthetic spectrum, we compare their intensities based on the following criterion. Outside of the plasma peak region $f \in [0.9,1.1]f_p$, the precision of the theory is considered to be very high, both below and above f_p. Here, the criterion for selecting channels to use for the fit is determined by the instrument data acquisition uncertainty. The frequency channels selected from V^2_{TNR} are only those with amplitudes within 10% of V^2. The confidence of both theory and measurements dramatically decreases very close to f_p and can also be strongly affected by a very small number of very fast, superhalo electrons (see, e.g., Chateau & Meyer-Vernet, 1991; Meyer-Vernet et al., 2017). To overcome this difficulty, we set the allowed difference between V^2_{TNR} and V^2 to scale linearly, being 10% at $0.9f_p$ and at $1.3f_p$, while

$$\left(\frac{V^2_{\mathrm{TNR}}}{V^2}\right)_{\max} = 1 + \frac{V^2_{\mathrm{TNR}}[p] - V^2_{\mathrm{TNR}}[i_{\min}]}{20\ \mathrm{dB}}, \tag{A1}$$

at f_p, where $\left(\frac{V^2_{\mathrm{TNR}}}{V^2}\right)_{\max}$ is the maximum allowed ratio between V^2_{TNR} and V^2 and $V^2_{\mathrm{TNR}}[p]$ and $V^2_{\mathrm{TNR}}[i_{\min}]$ are measured intensities of the peak and the signal minimum in $f < f_p$ region, respectively.

The global QF is given as a weighted average comprised of four components, defined as follows:

1. $\mathrm{QF}_{\mathrm{points}}$ signals the number of points that are close to the theoretical spectrum within the given criterion, divided by 48 (half of the total number of frequency channels). This value can be larger than 1, but this is never the case for real measurements (Figure 4).
2. $\mathrm{QF}_{\mathrm{peak}}$ quantifies the clearness/visibility of the peak by counting how many descending points at frequencies above $V^2_{\mathrm{TNR}}[p]$ and dividing that number by 20. This value can be higher than 1, but not lower than 0.2 due to the peak selection criteria given by Equation 2.
3. $\mathrm{QF}_{\mathrm{shift}}$ is calculated as $\mathrm{QF}_{\mathrm{shift}} = 1 - 10 < \sigma >$, where $<\sigma>$ is the rms of the difference between measured and theoretical spectrum, given as

$$\sigma(f) = \frac{V^2_{\mathrm{TNR}}(f)}{V^2(f)} - 1. \tag{A2}$$

This value can be negative due to the filtering tolerance around the peak, given by Equation A1.

4. $\mathrm{QF}_{\mathrm{lowlevel}}$ is the fraction of selected data points for which $V^2_{\mathrm{TNR}} > V^2$.

The total quality flag is calculated as

$$\mathrm{QF} = 5\mathrm{QF}_{\mathrm{points}} + 3\mathrm{QF}_{\mathrm{peak}} + \mathrm{QF}_{\mathrm{shift}} + \mathrm{QF}_{\mathrm{lowlevel}}, \tag{A3}$$

with a practical maximum value of 10. Due to $\mathrm{QF}_{\mathrm{peak}}$ possibly being larger than 1, QF can be larger than 10, but these spectra are extremely rare and we consider QF = 10 as the highest realistic value.

When the theoretical spectrum is above the measured one at any data point, with the tolerance defined in Equation A1, the QF for the associated spectrum is disregarded and is not considered for further analysis, as described in Section 2. There are also few other modifiers to the QF:

1. If n_e is more than 25% different than the value of $n_p + 2n_\alpha$, where n_p and n_α are proton and alpha densities measured by the Wind Faraday cups, the spectrum is not disregarded, but the QF is decreased by 1. The condition defined in Equation 2 is then modified to

$$V^2_{\mathrm{TNR}}[p] > V^2_{\mathrm{TNR}}[p-2] + 1\ \mathrm{dB}. \tag{A4}$$

These are a practical minimum difference found empirically, while its realistic value is 1.5–4 dB.

2. If data points $V^2_{\mathrm{TNR}}[p]$ and $V^2_{\mathrm{TNR}}[p-1]$ are not selected by the algorithm, they are artificially added to the filtered spectrum. These points are considered when calculating $\mathrm{QF}_{\mathrm{points}}$ and $\mathrm{QF}_{\mathrm{shift}}$, but not $\mathrm{QF}_{\mathrm{lowlevel}}$.
3. If there is not at least one filtered point both below $V^2_{\mathrm{TNR}}[p-1]$ or above $V^2_{\mathrm{TNR}}[p+2]$, the spectrum is disregarded.
4. If difference in the QTN intensity is larger than 1,000% at the boundary between TNR bands

$$\left(|V^2_{\mathrm{TNR}}[31] - V^2_{\mathrm{TNR}}[32]| > 10\mathrm{dB}\right) \vee \left(|V^2_{\mathrm{TNR}}[63] - V^2_{\mathrm{TNR}}[64]| > 10\ \mathrm{dB}\right), \tag{A5}$$

it is recognized as the instrument Automatic Gain Control issue and the spectrum is disregarded (this feature is diagnosed in a personal communication with the instrument team).

5. If $QF_{points} < 0.2$ the spectrum is disregarded as we require the number of degrees of freedom in the fit to be larger than the number of free parameters.

Data Availability Statement

SWE and 3DP data sets are available at NASA CDAWeb repository, at *wi_h1_swe* and *wi_emfits_e0_3dp* data sets, respectively. Wind Waves TNR L2 Dynamic Spectra is available at Wind Waves instrument section at CNES CDPP repository https://cdpp-archive.cnes.fr/.

Acknowledgments
M. M. Martinović, K. G. Klein, and H. Jain were financially supported by NASA grant 80NSSC19K0521. S. R. Gramze was financially supported by Arizona Space Grant AY2019-20.

References

Andronov, A. A. (1966). Antenna (Probe) Impedance and Noise in a Space Plasma. *Cosmic Research*, *4*, 493.
Bale, S. D., Goetz, K., Harvey, P. R., Turin, P., Bonnell, J. W., Dudok de Wit, T., et al. (2016). The fields instrument suite for solar probe plus - measuring the coronal plasma and magnetic field, plasma waves and turbulence, and radio signatures of solar transients. *Space Science Reviews*, *204*, 49–82.
Balmain, K. (1969). Dipole admittance for magnetoplasma diagnostics. *IEEE Transactions on Antennas and Propagation*, *17*, 389–392.
Bame, S. J., Asbridge, J. R., Felthauser, H. E., Glore, J. P., Hawk, H. L., & Chavez, J. (1978). ISEE-C solar wind plasma experiment. *IEEE Transactions on Geoscience Electronics*, *16*, 160–162. https://doi.org/10.1109/TGE.1978.294538
Berčič, L., Maksimović, M., Land i, S., & Matteini, L. (2019). Scattering of strahl electrons in the solar wind between 0.3 and 1 au: Helios observations. *Monthly Notices of the Royal Astronomical Society*, *486*(3), 3404–3414. https://doi.org/10.1093/mnras/stz1007
Bougeret, J. L., Kaiser, M. L., Kellogg, P. J., Manning, R., Goetz, K., Monson, S. J., et al. (1995). Waves: The radio and plasma wave investigation on the Wind spacecraft. *Space Science Reviews*, *71*, 231–265.
Bowen, T. A., Badman, S., Hellinger, P., & Bale, S. D. (2018). Density Fluctuations in the Solar Wind Driven by Alfvén Wave Parametric Decay. *Astrophysical Journal Letters*, *854*(2), L33. https://doi.org/10.3847/2041-8213/aaabbe
Cairns, I. H. (1986). New waves at multiples of the plasma frequency upstream of the Earth's bow shock. *Journal of Geophysical Research*, *91*(A3), 2975–2988. https://doi.org/10.1029/JA091iA03p02975
Chateau, Y. F., & Meyer-Vernet, N. (1989). Electrostatic noise in non-Maxwellian plasmas: Flat-top distribution function. *Journal of Geophysical Research*, *94*, 15,407–15,414.
Chateau, Y. F., & Meyer-Vernet, N. (1991). Electrostatic noise in non-Maxwellian plasmas: Generic properties and 'kappa' distributions. *Journal of Geophysical Research*, *96*, 5825–5836.
Chen, C. H. K., Sorriso-Valvo, L., Šafránková, J., & Němeček, Z. (2014). Intermittency of solar wind density fluctuations From ion to electron scales. *Astrophysical Journal Letters*, *789*(1), L8. https://doi.org/10.1088/2041-8205/789/1/L8
Couturier, P., Meyer-Vernet, N., Hoang, S., & Steinberg, J. L. (1981). Quasi-thermal noise in a stable plasma at rest: Theory and observations from ISEE 3. *Journal of Geophysical Research*, *86*, 11,127–11,138.
Fejer, J. A., & Kan, J. R. (1969). Noise spectrum received by an antenna in a plasma. *Radio Science*, *4*, 721–728.
Feldman, W. C., Anderson, R. C., Bame, S. J., Gary, S. P., Gosling, J. T., McComas, D. J., et al. (1983). Electron velocity distributions near the Earth's bow shock. *Journal of Geophysical Research*, *88*(A1), 96–110. https://doi.org/10.1029/JA088iA01p00096
Gosling, J. T., Baker, D. N., Bame, S. J., Feldman, W. C., Zwickl, R. D., & Smith, E. J. (1987). Bidirectional solar wind electron heat flux events. *Journal of Geophysical Research*, *92*, 8519–8535.
Henri, P., Meyer-Vernet, N., Briand, C., & Donato, S. (2011). Observations of Langmuir ponderomotive effects using the solar terrestrial relations observatory spacecraft as a density probe. *Physics of Plasmas*, *18*, 82308.
Hillan, D. S., Cairns, I. H., Robinson, P. A., & Mohamed, A. (2010). Prediction of background levels for the Wind WAVES instrument and implications for the galactic background radiation. *Journal of Geophysical Research*, *115*, A06102. https://doi.org/10.1029/2009JA014714
Hull, A. J., Scudder, J. D., Frank, L. A., Paterson, W. R., & Kivelson, M. G. (1998). Electron heating and phase space signatures at strong and weak quasi-perpendicular shocks. *Journal of Geophysical Research*, *103*(A2), 2041–2054. https://doi.org/10.1029/97JA03058
Issautier, K., Meyer-Vernet, N., Moncuquet, M., & Hoang, S. (1996). A novel method to measure the solar wind speed. *Geophysical Research Letters*, *23*, 1649–1652.
Issautier, K., Meyer-Vernet, N., Moncuquet, M., & Hoang, S. (1999). Quasi-thermal noise in a drifting plasma: Theory and application to solar wind diagnostic on Ulysses. *Journal of Geophysical Research*, *104*, 6691–6704.
Issautier, K., Perche, C., Hoang, S., Maksimović, M., Lacombe, C., Bougeret, J.-L. H., & Salem, C. (2005). Solar wind electron density and temperature over solar cycle 23: Thermal noise measurements on wind. *Advances in Space Research*, *35*, 2141–2146.
Kellogg, P. (1981). Calculation and observation of thermal electrostatic noise in solar wind plasma. *Plasma Physics*, *23*, 735–751.
Kellogg, P. J., Goetz, K., Monson, S. J., Bale, S. D., Reiner, M. J., & Maksimović, M. (2009). Plasma wave measurements with stereo s/waves: Calibration, potential model, and preliminary results. *Journal of Geophysical Research*, *114*, A02107. https://doi.org/10.1029/2008JA013566
Laframboise, J. G., & Parker, L. W. (1973). Probe design for orbit-limited current collection. *The Physics of Fluids*, *16*, 629–636.
Le Chat, G., Issautier, K., Meyer-Vernet, N., & Hoang, S. (2011). Large-scale variation of solar wind electron properties from quasi-thermal noise spectroscopy: Ulysses measurements. *Solar Physics*, *271*, 141–148.
Le Chat, G., Issautier, K., Meyer-Vernet, N., Zouganelis, Y., Maksimović, M., & Moncuquet, M. (2009). Quasi-thermal noise in space plasma: 'Kappa' distributions. *Physics of Plasmas*, *16*, 102,903.
Le Chat, G., Zaslavsky, A., Meyer-Vernet, N., Issautier, K., Belheouane, S., Zouganelis, Y., et al. (2013). Interplanetary nanodust detection by the solar terrestrial relations observatory/waves low frequency receiver. *Solar Physics*, *286*, 549–559.
Lin, R. P., Anderson, K. A., Ashford, S., Carlson, C., Curtis, D., Ergun, R., et al. (1995). A three-dimensional plasma and energetic particle investigation for the Wind spacecraft. *Space Science Reviews*, *71*, 125–153.
Maksimović, M., Bale, S. D., Chust, T., Khotyaintsev, Y., Krasnoselskikh, V., Kretzschmar, M., et al. (2020). The solar orbiter radio and plasma waves (rpw) instrument. *Astronomy & Astrophysics*. https://doi.org/10.1051/0004-6361/201936214
Maksimovic, M., Bougeret, J. L., Perche, C., Steinberg, J. T., Lazarus, A. J., ViÃśas, A. F., & Fitzenreiter, R. J. (1998). Solar wind density intercomparisons on the WIND spacecraft using WAVES and SWE experiments. *Geophysical Research Letters*, *25*, 1265–1268.

Maksimovic, M., Hoang, S., Meyer-Vernet, N., Moncuquet, M., Bougeret, J. L., Phillips, J. L., & Canu, P. (1995). Solar wind electron parameters from quasi-thermal noise spectroscopy and comparison with other measurements on Ulysses. *Journal of Geophysical Research*, *100*(A10), 19,881–19,892. https://doi.org/10.1029/95JA01550

Maksimović, M., Issautier, K., Meyer-Vernet, N., Perche, C., Moncuquet, M., Zouganelis, Y., et al. (2005). Solar wind electron temperature and density measurements on the solar orbiter with thermal noise spectroscopy. *Advances in Space Research*, *35*, 1471–1473.

Maksimović, M., Pierrard, V., & Lemaire, J. F. (1997). A kinetic model of the solar wind with kappa distribution functions in the corona. *Astronomy and Astrophysics*, *324*, 725–734.

Martinović, M. M. (2016). A study of quasi-thermal noise and shot noise in space plasmas (Unpublished doctoral dissertation), LESIA, Observatoire de Paris/University of Belgrade. https://doi.org/10.5281/zenodo.3592084

Martinović, M. M., Zaslavsky, A., Maksimović, M., & Åacegan, S. (2017). Electrostatic thermal noise in a weakly ionized collisional plasma. *Radio Science*, *52*, 70–77. https://doi.org/10.1002/2016RS006189

Martinović, M. M., Zaslavsky, A., Maksimović, M., & Issautier, K. (2017). Quasi-thermal noise spectroscopy in Earth's magnetosheath: Theory and application to plasma diagnostic on Wind spacecraft. *Publications of the Astronomical Observatory of Belgrade*, *96*, 141–146.

Martinović, M. M., Zaslavsky, A., Maksimović, M., Meyer-Vernet, N., Åacegan, S., Zouganelis, Y., et al. (2016). Quasi-thermal noise measurements on stereo: Kinetic temperature deduction using electron shot noise model. *Journal of Geophysical Research: Space Physics*, *121*, 129–139. https://doi.org/10.1002/2015JA021710

Martinović, M. M., Zaslavsky, A., Maksimovic, M., Šegan, S., & Svetlik, M. (2015). Quasi-thermal noise observed by CASSINI during the first flyby of Venus, *AGU Fall Meeting Abstracts* (Vol. 2015, pp. SH31C–2433). San Francisco, USA.

Meyer-Vernet, N. (1979). On natural noises detected by antennas in plasmas. *Journal of Geophysical Research*, *94*, 2405–2415.

Meyer-Vernet, N. (1982). Flip-flop of electric potential of dust grains in space. *Astronomy and Astrophysics*, *105*, 98–106.

Meyer-Vernet, N. (1983). Quasi-thermal noise correction due to particle impacts of emission. *Journal of Geophysical Research*, *88*, 8081–8093.

Meyer-Vernet, N., Couturier, P., Hoang, S., Steinberg, J. L., & Zwickl, R. D. (1986). Ion thermal noise in the solar wind - interpretation of the 'excess' electric noise on isee 3. *Journal of Geophysical Research*, *91*, 3294–3298.

Meyer-Vernet, N., Hoang, S., & Moncuquet, M. (1993). Bernstein waves in the io plasma torus: A novel kind of electron temperature sensor. *Journal of Geophysical Research*, *98*, 21,163–21,176.

Meyer-Vernet, N., Issautier, K., & Moncuquet, M. (2017). Quasi-thermal noise spectroscopy: The art and the practice. *Journal of Geophysical Research: Space Physics*, *122*, 7925–7945. https://doi.org/10.1002/2017JA024449

Meyer-Vernet, N., & Perche, C. (1989). Tool kit for antennae and thermal noise near the plasma frequency. *Journal of Geophysical Research*, *94*, 2405–2415.

Moncuquet, M., Meyer-Vernet, N., & Hoang, S. (1995). Dispersion of electrostatic waves in the Io plasma torus and derived electron temperature. *Journal of Geophysical Research*, *100*, 2373–2379.

Moncuquet, M., Meyer-Vernet, N., & Hoang, S. (1997). Detection of Bernstein wave forbidden bands in the Jovian magnetosphere: A new way to measure the electron density. *Journal of Geophysical Research*, *102*, 21,697–21,708.

Moncuquet, M., Meyer-Vernet, N., Issautier, K., Pulupa, M., Bonnell, J. W., Bale, S. D., et al. (2020). First in situ measurements of electron density and temperature from quasi-thermal noise spectroscopy with Parker Solar Probe/FIELDS. *The Astrophysical Journal Supplement Series*, *246*(2), 44. https://doi.org/10.3847/1538-4365/ab5a84

Morse, R. L. (1965). Adiabatic time development of plasma sheaths. *Physics of Fluids*, *8*(2), 308–314. https://doi.org/10.1063/1.1761224

Ogilvie, K. W., Chornay, D. J., Fritzenreiter, R. J., Hunsaker, F., Keller, J., Lobell, J., et al. (1995). SWE: A comprehensive plasma instrument for the Wind spacecraft. *Space Science Reviews*, *71*(1-4), 55–77. https://doi.org/10.1007/BF00751326

Pulupa, M., Bale, S. D., Salem, C., & Horaites, K. (2014). Spin-modulated spacecraft floating potential: Observations and effects on electron moments. *Journal of Geophysical Research: Space Physics*, *119*, 647–657. https://doi.org/10.1002/2013JA019359

Salem, C., Bosqued, J.-M., Larson, D. E., Mangeney, A., Maksimović, M., Perche, C., et al. (2003). Determination of accurate solar wind electron parameters using particle detectors and radio wave receivers. *Journal of Geophysical Research*, *106*, 21,701–21,717.

Salem, C., Hoang, K., Sang, I., Maksimović, M., & Perche, C. (2003). Wind-Ulysses in-situ thermal noise measurements of solar wind electron density and core temperature at solar maximum and minimum. *Advances in Space Research*, *32*, 491–496.

Salem, C., Lacombe, C., Mangeney, A., Kellogg, P. J., & Bougeret, J. L. (2003). Weak double layers in the solar wind and their relation to the interplanetary electric field. In M. Velli, R. Bruno, & F. Malara (Eds.), *Solar wind ten* (Vol. 679, pp. 513–517). Pisa, Italy. https://doi.org/10.1063/1.1618647

Sauvaud, J. A., Larson, D., Aoustin, C., Curtis, D., MÃl'dale, J. L., Fedorov, A., et al. (2008). The impact solar wind electron analyzer (SWEA). *Space Science Reviews*, *136*, 227–239.

Schwenn, R., Rosenbauer, H., & Miggenrieder, H. (1975). The plasma experiment on board Helios /E 1/. *Raumfahrtforschung*, *19*, 226–232.

Sentman, D. D. (1982). Thermal fluctuations and the diffuse electrostatic emissions. *Journal of Geophysical Research*, *87*, 1455–1472.

Spann, J., Burkepile, J., Coster, A., Florinski, V., Klumpar, D., Kucharek, H., et al. (2017). The 2017 senior review of the Heliophysics Operating Missions.

Štverak, S., Maksimović, M., Travniíček, P., Marsch, E., Fazakerley, A. N., & Scime, E. E. (2009). Radial evolution of nonthermal electron populations in the low-latitude solar wind: Helios, Cluster, and Ulysses observations. *Journal of Geophysical Research*, *114*, A05104. https://doi.org/10.1029/2008JA013883

Tong, Y., Pulupa, M., Salem, C., & Bale, S. D. (2015). Investigating wind quasi-thermal noise spectra between the ion and the electron plasma frequency. *AGU Fall Meeting Abstracts*, SH11D-2401.

Vidojević, S., Zaslavsky, A., Maksimović, M., Dražić, M., & Atanacković, O. (2011). Statistical analysis of Langmuir waves associated with type III radio bursts: I. Wind observations. *Baltic Astronomy*, *20*, 596–599. https://doi.org/10.1515/astro-2017-0343

Whipple, J., Elden, C., & Parker, L. W. (1969). Effects of secondary electron emission on electron trap measurements in the magnetosphere and solar wind. *Journal of Geophysical Research*, *74*(24), 5763. https://doi.org/10.1029/JA074i024p05763

Whittlesey, P. L., Larson, D. E., Kasper, J. C., Halekas, J., Abatcha, M., Abiad, R., et al. (2020). The Solar Probe ANalyzers–Electrons on the Parker Solar Probe. *Astrophysical Journal Supplement Series*, *246*(2), 74. https://doi.org/10.3847/1538-4365/ab7370

Wilson, I., Lynn, B., Chen, L.-J., Wang, S., Schwartz, S. J., Turner, D. L., et al. (2019). Electron energy partition across interplanetary shocks. I. Methodology and Data Product. *The Astrophysical Journal Supplement Series*, *243*(1), 8. https://doi.org/10.3847/1538-4365/ab22bd

Wilson, I., Lynn, B., Chen, L.-J., Wang, S., Schwartz, S. J., Turner, D. L., et al. (2019). Electron energy partition across interplanetary shocks. II. Statistics. *The Astrophysical Journal Supplement Series*, *245*(2), 24. https://doi.org/10.3847/1538-4365/ab5445

Young, D. T., Berthelier, J. J., Blanc, M., Burch, J. L., Coates, A. J., Goldstein, R., et al. (2004). Cassini plasma spectrometer investigation. *Space Science Reviews*, *114*(1-4), 1–112. https://doi.org/10.1007/s11214-004-1406-4

Zouganelis, Y. (2008). Measuring suprathermal electron parameters in space plasmas: Implementation of the quasi-thermal noise spectroscopy with kappa distributions using in situ Ulysses/URAP radio measurements in the solar wind. *Journal of Geophysical Research*, *113*, A08111. https://doi.org/10.1029/2007JA012979

Zouganelis, Y., Maksimović, M., Meyer-Vernet, N., Bale, S. D., Eastwood, J. P., Zaslavsky, A., et al. (2010). Measurements of stray antenna capacitance in the stereo/waves instrument: Comparison of the measured voltage spectrum with an antenna electron shot noise model. *Radio Science*, *45*, 1005–1009. https://doi.org/10.1029/2009RS004194